ADVANCING EARTH AND SPACE SCIENCES

JGR Atmospheres

RESEARCH ARTICLE
10.1029/2023JD039751

Key Points:

- Cloud phase heterogeneity is greatest at −5°C, when small ice patches form in majority-liquid clouds
- Cloud phase is relatively homogeneous over the Southern Ocean and heterogeneous over the northern continents
- For a fixed temperature, extratropical phase heterogeneity is generally greatest during local spring and summer

Supporting Information:

Supporting Information may be found in the online version of this article.

Correspondence to:

A. B. Sokol,
abs66@uw.edu

Citation:

Sokol, A. B., & Storelvmo, T. (2024). The spatial heterogeneity of cloud phase observed by satellite. *Journal of Geophysical Research: Atmospheres*, *129*, e2023JD039751. https://doi.org/10.1029/2023JD039751

Received 9 AUG 2023
Accepted 23 JAN 2024

The Spatial Heterogeneity of Cloud Phase Observed by Satellite

Adam B. Sokol[1,2] and Trude Storelvmo[2]

[1]Department of Atmospheric Sciences, University of Washington, Seattle, WA, USA, [2]Department of Geosciences, University of Oslo, Oslo, Norway

Abstract We conduct a global assessment of the spatial heterogeneity of cloud phase within the temperature range where liquid and ice can coexist. Single-shot Cloud-Aerosol Lidar with Orthogonal Polarization lidar retrievals are used to examine cloud phase at scales as fine as 333 m, and horizontal heterogeneity is quantified according to the frequency of switches between liquid and ice along the satellite's path. In the global mean, heterogeneity is greatest between −15 and −4°C with a peak at −5°C, when small patches of ice are prevalent within liquid-dominated clouds. Heterogeneity "hot spots" are typically found over the extratropical continents, whereas phase is relatively homogeneous over the Southern Ocean and the eastern subtropical ocean basins, where supercooled liquid clouds dominate. Even at a fixed temperature, heterogeneity undergoes a pronounced annual cycle that, in most places, consists of a minimum during autumn or winter and a maximum during spring or summer. Based on this spatial and temporal variability, it is hypothesized that heterogeneity is affected by the availability of ice nucleating particles. These results can be used to improve the representation of subgrid-scale heterogeneity in general circulation models, which has the potential to reduce longstanding model biases in cloud phase partitioning and radiative fluxes.

Plain Language Summary At temperatures where ice and liquid can coexist within clouds, climate models tend to produce too much ice and too little liquid compared to satellite observations. This bias is likely caused by the assumption that liquid and ice are uniformly mixed, which results in the rapid conversion of liquid to ice for thermodynamic reasons. To reduce this bias, models need to account for the spatial heterogeneity ("patchiness") of liquid and ice that exists in the real atmosphere. The goal of this paper is to quantify this spatial heterogeneity using satellite-based lidar observations of cloud phase. We find small pockets of ice in liquid-dominated clouds to be more common than small pockets of liquid in ice-dominated clouds. The greatest heterogeneity is found over the midlatitude continents, whereas phase is relatively uniform over the Southern Ocean and other maritime regions with extensive low cloud cover. In the mid and high latitudes, cloud phase tends to be more heterogeneous during spring and summer and more homogeneous during autumn and winter. These results can be used in the future to improve model representations of the thermodynamic processes responsible for biases in cloud phase.

1. Introduction

Cloud feedbacks remain a leading source of uncertainty in estimates of climate sensitivity (Sherwood et al., 2020; Zelinka et al., 2020). One such feedback is the cloud phase feedback, which was first described by Mitchell et al. (1989) as a negative feedback resulting from a shift in cloud phase partitioning from ice to liquid with warming. The feedback is negative because liquid cloud droplets are generally smaller and more numerous than ice crystals, which means that liquid clouds are optically thicker than ice clouds of the same condensate mass. A shift in phase partitioning from ice to liquid therefore produces an increase in cloud albedo.

The magnitude of the cloud phase feedback has proved tricky to constrain using models, largely because of its sensitivity to the phase partitioning of the initial state (Choi et al., 2014; Storelvmo et al., 2015; Tsushima et al., 2006). General circulation models (GCMs) systematically produce too much ice and too little liquid within the mixed-phase temperature range (−40° to 0°), especially over the Southern Ocean (SO) (Cesana et al., 2015; Kay et al., 2016; Komurcu et al., 2014). As a result, present-day cloud albedo is too low in many GCM simulations, and the albedo enhancement associated with ice-to-liquid transitions is too dramatic. Adjustment of present-day phase partitioning to more closely match observations results in a weakened cloud phase feedback and an increase in simulated climate sensitivity (Frey & Kay, 2018; Tan et al., 2016). While these biases have

been significantly mitigated in the most recent phase of the Coupled Model Intercomparison Project (Zelinka et al., 2020), representing phase partitioning in a physically informed manner remains a challenge.

Biases in phase partitioning are thought to be caused, at least in part, by an overactive Wegener-Bergeron-Findeisen (WBF) process (McIlhattan et al., 2017; Tan & Storelvmo, 2016). The WBF process is a consequence of the difference in saturation vapor pressures with respect to liquid and ice, which, in a mixed-phase environment, can cause ice crystals to grow at the expense of nearby liquid droplets (Bergeron, 1928; Findeisen, 1938; Wegener, 1911). GCM parameterizations of the WBF process typically assume that liquid and ice are homogeneously mixed throughout a model grid box, which allows for efficient WBF glaciation of supercooled liquid. But aircraft observations, while limited, suggest that mixed-phase clouds often contain discrete liquid-only and ice-only pockets much smaller than a GCM grid box (Chylek & Borel, 2004; Field et al., 2004; Korolev et al., 2003). By reducing the spatial overlap of ice and liquid condensate, this heterogeneity could limit WBF efficiency in the real atmosphere, and previous work has shown that accounting for heterogeneity can mitigate model biases in phase partitioning (Huang et al., 2021; Tan & Storelvmo, 2016; Zhang et al., 2019). An important takeaway from this previous work is that there is no one-size-fits-all adjustment to WBF efficiency that improves model phase biases across time and space: the sensitivity of phase biases to WBF efficiency varies with location, season, and temperature, and this variability presumably reflects different degrees of phase heterogeneity in the real world. Attempts to reduce model phase biases, if they are to be physically grounded, must therefore account not only for the existence of phase heterogeneity but also for its spatial and temporal variability.

Understanding phase heterogeneity in the real atmosphere is a difficult problem because it occurs on scales ranging from microns to kilometers (Atlas et al., 2021; Korolev et al., 2003). Capturing this range of scales requires in situ aircraft observations, which typically have a measurement frequency of 1 Hz (every 100–200 m, depending on aircraft speed). Studies making use of these measurements have generally shown that a relatively small portion of 1-Hz observations within the mixed-phase temperature range contain both liquid and ice; most are single-phase or heavily dominated by one phase or the other (D'Alessandro et al., 2019, 2021; Field et al., 2004; Korolev et al., 2003; Zhang et al., 2019). On the whole, these studies suggest that mixed-phase conditions at the 100-m scale are relatively rare. This is not surprising given that mixtures of liquid and ice are thermodynamically unstable, which is what gives rise to the WBF process in the first place. Nevertheless, these observational assessments come with considerable uncertainty arising from imperfect phase classification algorithms, varied definitions of "mixed-phase," and various instrument limitations (Baumgardner et al., 2017; McFarquhar et al., 2013). Perhaps most importantly, aircraft observations are limited in number, and the generalizability of existing observations is unknown.

Spaceborne satellite observations are a largely untapped resource for studying cloud phase heterogeneity. Thompson et al. (2018) assessed phase heterogeneity at cloud top using retrievals from the Hyperion spectrometer, but the spatial coverage of the observations was very sparse, and they were limited to daytime hours. These limitations can be largely overcome by polar-orbiting satellites with active sensors, which offer near-global coverage over extended periods of time and can penetrate below cloud top until their signal is attenuated. While these satellites cannot capture the fine spatial scales observable by aircraft and Hyperion, the aircraft observations discussed previously suggest that a resolution of a few hundred meters can capture a large portion of cloud phase variability. For these reasons, we believe active-sensing satellites are a promising avenue for understanding phase heterogeneity on a global scale and improving its representation in models.

The goal of this work is to quantify cloud phase heterogeneity, its temperature dependence, and its spatiotemporal variability using spaceborne lidar measurements. In Section 2, we describe the lidar observations and develop a metric used to quantify phase heterogeneity in the satellite record. Results are presented in Section 3 and discussed in Section 4.

2. Data and Methods

2.1. Observational Data

Observations of cloud phase are obtained from the Cloud-Aerosol Lidar with Orthogonal Polarization (CALIOP) aboard the polar-orbiting CALIPSO satellite (Winker et al., 2009). The reasons for using CALIOP are its near-global coverage and its relatively high horizontal resolution: single-shot profiles of the atmosphere have a vertical resolution of 30 m, a horizontal footprint of 90 m, and are recorded every 333 m along the satellite's

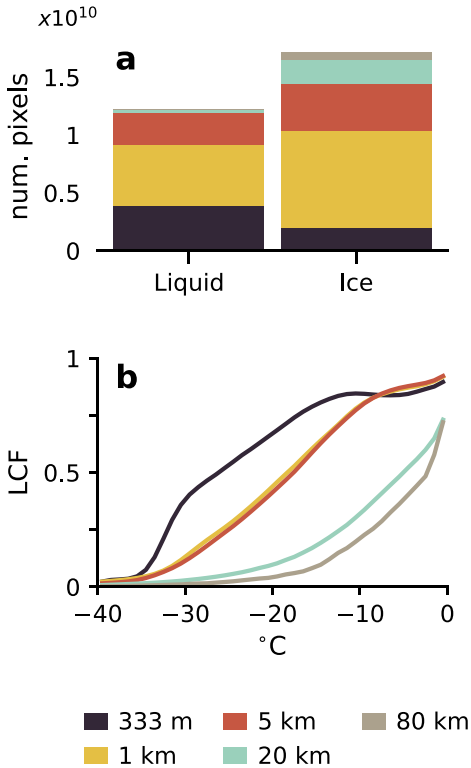

Figure 1. Statistics of the cloud phase retrievals used in this analysis. (a) Number of pixels sorted by averaging length L and retrieved cloud phase; (b) liquid cloud fraction (LCF) as a function of L and temperature. Values in (a) reflect the number of pixels at the single-shot resolution, even if the phase determinations required averaging at a greater spatial scale. The ice category includes both randomly and horizontally oriented ice. Only medium- and high-quality phase determinations are included, and all data are from below 8.2 km.

path. We take data from the L2 Vertical Feature Mask (VFM) product (v4.20; NASA/LARC/SD/ASDC, 2018a), which provides retrieved cloud phase at the single-shot resolution up to an altitude of 8.2 km. Temperature data are obtained from GEOS-5 reanalysis via the CALIOP L2 Cloud Profile product (v4.20; NASA/LARC/SD/ASDC, 2018b) and are interpolated onto the same single-shot grid used for the phase data. Interpolation onto the single-shot grid captures the large-scale thermal structure of the atmosphere but likely fails to capture small-scale temperature variations. The study period is from 1 December 2009 to 30 November 2012. To reduce specular reflection from horizontally oriented ice particles, the CALIPSO viewing angle was 3° off-nadir at this time.

In the CALIOP retrievals used here, cloud layer phase is determined based on the layer-integrated attenuated backscatter at 532 nm and depolarization ratio (Avery et al., 2020; Hu et al., 2009). Cloudy volumes are classified as liquid, randomly oriented ice, horizontally oriented ice, or unknown phase. Each phase determination is accompanied by a quality indicator, which we use to eliminate low-confidence determinations. For our study period, this removes 17% of all cloudy pixels. As with any remotely retrieved quantity, the phase retrievals have several limitations. First, the phase classification scheme does not include a mixed-phase category despite the fact that mixed-phase conditions are known to occur on length scales smaller than 333 m (Atlas et al., 2021; Field et al., 2004). In such conditions, it is difficult to detect ice by lidar since the number concentration of ice crystals is generally much lower than that of supercooled liquid droplets (Mace et al., 2021). As a result, many mixed-phase cloud scenes are likely classified as liquid.

A second limitation is that multiple single-shot profiles must often be averaged together before any cloud-related backscatter signal can be distinguished from background noise (Vaughan et al., 2009; Winker et al., 2009). For this reason, the CALIOP retrievals use an automated, multi-gridded cloud layer detection scheme that is thoroughly described in Vaughan et al. (2005, 2009). The scheme passes through the data multiple times with varying degrees of horizontal averaging; we refer to this along-track averaging length as L. Cloud features can be identified during any one of these passes, and cloud phase is retrieved at the same resolution that the feature was identified with. For the first pass, fifteen single-shot profiles are averaged into a 5-km chunk before the feature detection algorithm is applied. If a cloud feature is identified, two subsequent passes are done, one with $L = 1$ km and another at the 333-m single-shot resolution. If any features detected at $L = 333$ m are within the surface boundary layer, they are removed from the 5-km chunk and 5-km layer properties are recalculated; this cloud-clearing procedure is not applied if features are detected at $L = 333$ m in all 15 shots within a 5-km chunk. Lastly, two more passes are done using 20- and 80-km chunks, in which finer features are removed before the feature properties are calculated. The implication of this scheme is that single-shot phase identifications can be embedded within broader features identified at greater L. For example, if a cloud layer is identified with $L = 5$ km (i.e., when 15 single-shot profiles are averaged together), a single phase retrieval is performed for the entire 5-km chunk, and the phase information is simply repeated in 15 consecutive, "single-shot" pixels in the VFM data product used here. Pixels within the 5-km chunk may be altered if finer cloud features of different phase are identified during the subsequent 1-km and 333-m scans.

An important consequence of the multi-gridded cloud-finding scheme is that adjacent phase retrievals are not always independent from one another. In fact, only 20% of the retrievals included in this analysis were made at the single-shot resolution; 47% were made with $L = 1$ km; 24% with $L = 5$ km; 7% with $L = 20$ km; and 2% with $L = 80$ km (Figure 1a). For this reason, we group cloudy pixels by their associated averaging length L and perform our phase heterogeneity analysis (described in Section 2.2) separately for each group. We exclude 20- and 80-km phase retrievals from our analysis, since they account for a small fraction of the total observations and are beyond our lengthscales of interest. The multi-gridded averaging also means that our results underestimate true phase heterogeneity and serve as a lower bound on heterogeneity at the single-shot (~333 m) scale.

In addition, the averaging length required to detect a cloud feature is itself dependent on cloud phase. Figure 1a shows the distribution of L for each liquid or ice pixel on the single-shot grid. In general, liquid clouds are detected at shorter averaging lengths. This is to be expected, since liquid clouds are, on average, optically thicker than ice clouds and produce a stronger backscatter signal. The disparity is especially clear for phase retrievals made at the single-shot resolution: two-thirds of these retrievals are liquid despite the fact that the liquid cloud fraction (LCF) is 0.43 for the entire set of pixels considered here. Here, LCF is simply the fraction of cloudy pixels with a phase identification that have been classified as liquid. Figure 1b shows how LCF varies with L and temperature; in general, LCF increases smoothly between −40 and 0°C, consistent with previous work (Cesana et al., 2016; Korolev et al., 2017). Across most of the mixed-phase temperature range, LCF generally decreases with increasing L, but the relationship is nonlinear: there is a large decrease in LCF as L increases from 333 m to 1 km, but very little change between 1 and 5 km. LCF is lower again for $L = 20$ km, but relatively similar for 20 and 80 km. Lastly, we note that the distribution of L may vary between day and night due to the greater level of background noise during the day; exploring this diurnal sensitivity is beyond our scope here.

2.2. Quantification of Phase Heterogeneity

Previous work has quantified phase heterogeneity based on the frequency of switches between liquid and ice along an aircraft flight track or on the horizontal extent of single-phase patches within a cloud (Atlas et al., 2021; D'Alessandro et al., 2021). We take a similar approach with the satellite observations. We define the *interface density* I [km^{-1}] as the number of switches between liquid and ice per horizontal kilometer of cloud along the satellite track. To compute I, we compare immediately adjacent phase observations at the same vertical level. The boundary between two pixels is considered to be a liquid-ice interface only if one of the pixels is liquid and the other is ice (either randomly or horizontally oriented) and only if both phase determinations are of medium or high confidence. Each cloud observation is assigned a "heterogeneity score" equal to the number of liquid-ice interfaces at its horizontal edges (0, 1, or 2; Figures 2b and 2c). The averaging length required to make the phase retrieval has not been considered up to this stage.

Once pixels have been assigned a value of 0, 1, or 2, they are sorted by temperature (1°C bins), latitude (5° bins), longitude (10° bins), month, and averaging length L. For each subset of observations, we then compute I as

$$I = \frac{(N_1/2 + N_2)}{N_c \cdot \Delta x} \tag{1}$$

where Δx is the horizontal resolution of the retrieval grid (0.333 km), N_x is the number of cloud observations in the subset with a heterogeneity score of x, and $N_c = N_0 + N_1 + N_2$ is the total number of cloud observations in the subset (excluding low-confidence retrievals). N_1 is scaled by a factor of 1/2 so that phase interfaces are not double-counted. The maximum possible value of I is 3 km^{-1} ($=1/\Delta x$), which would be achieved in the limiting case of an infinitely long cloud with alternating phase observations retrieved at the single-shot resolution. In this case, $N_c = N_2$.

Figure 2a illustrates our methodology for three schematic cloud transects. When I is large, cloud phase is more heterogeneous, single-phase cloud segments are shorter in length, and there is a greater contact area between liquid-only and ice-only patches. This is the case in transect #3, a mixed-phase cloud in which liquid and ice alternate with every pixel. Conversely, small I corresponds to large patches of uniform phase. This is the case in the all-liquid Transect #1, which represents the most homogeneous case. Transect #2 is a compromise between the extremes.

Furthermore, I can be computed separately for the liquid and ice-phase observations within each data subset. We refer to these quantities as I_{liq} and I_{ice}, which can be used to understand how the characteristic size of ice-only patches differs from that of liquid-only patches. I_{liq} and I_{ice} are related to I by

$$I = \mathrm{LCF} \cdot I_{liq} + (1 - \mathrm{LCF}) \cdot I_{ice} \tag{2}$$

When computing I_{liq} using Equation 1, N_x represents the number of *liquid* cloud observations, rather than total cloud observations, with a heterogeneity score of x. I_{ice} is computed in the same manner but using the number of ice observations. When I_{liq} is large, liquid cloud observations are more likely to be adjacent to ice cloud observations, meaning that liquid-only patches are relatively small; conversely, small I_{liq} corresponds to large

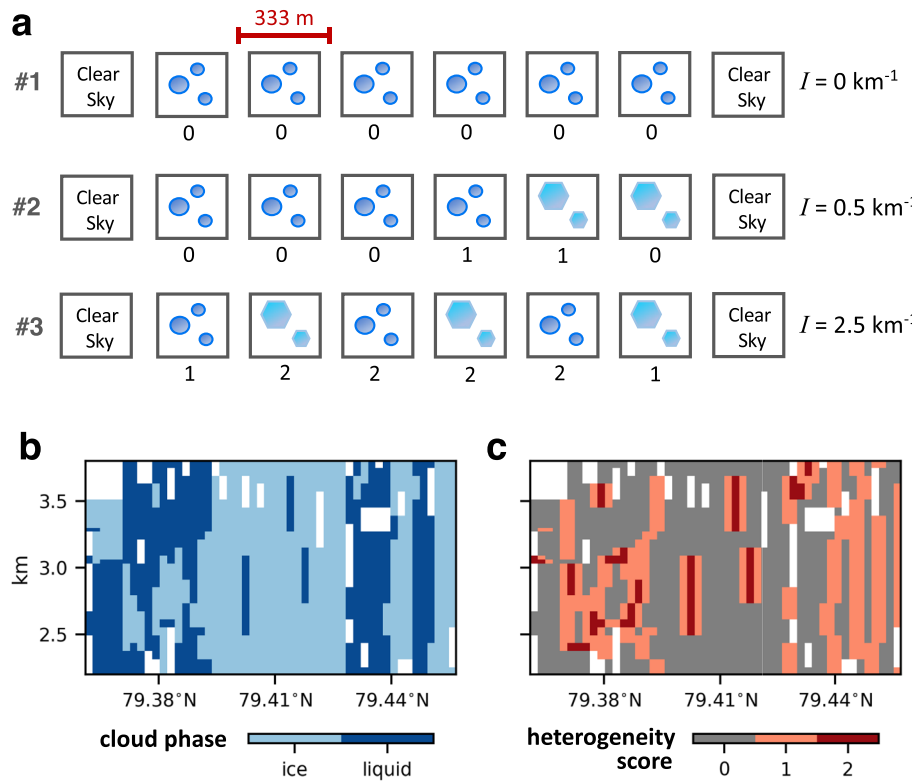

Figure 2. (a) Schematic illustrating the interface density metric, I, used to quantify cloud phase heterogeneity. Each box represents one single-shot lidar profile and its associated phase retrieval. For simplicity, we have assumed that each retrieval was made at the single-shot resolution ($L = 333$ m). The number below each pixel indicates the heterogeneity score of each pixel, equal to the number of horizontally adjacent phase interfaces. Circles represent liquid and hexagons represent ice. I is computed for each transect following Equation 1. (b) Retrieved cloud phase and (c) corresponding heterogeneity score for a 17-km section of the CALIPSO swath from 05:23:20 UTC on 21 May 2011.

liquid-only patches. For a set of cloud observations corresponding to a particular temperature range, time period, and/or latitude, the values of I, I_{liq}, I_{ice}, and LCF provide an informative description of cloud phase composition and heterogeneity.

The heterogeneity metrics described here only reflect horizontal heterogeneity. For our purpose of improving model representation of subgrid-scale heterogeneity, it is appropriate to neglect the vertical dimension, since the horizontal extent of a GCM gridbox is ~2 orders of magnitude larger than the vertical extent. Most of the interface area between liquid-ice within a grid box would therefore be expected to arise from horizontal heterogeneity. Moreover, the CALIOP cloud phase retrievals are performed using layer-integrated quantities, which means that vertically adjacent phase retrievals are seldom independent.

3. Results

3.1. Temperature Dependence

We first examine how phase heterogeneity varies with temperature. Figures 3a–3c shows global mean I as a function of temperature and averaging length. As expected, phase retrievals made at the single-shot resolution are the most heterogeneous, simply because they are more likely to be independent of adjacent retrievals. But the variations in I across the mixed-phase temperature range are qualitatively similar for all L, so we discuss them here in general terms. I is lowest near the homogeneous freezing point at −40°C, increases with temperature between −40 and −14°C, and remains high between −14 and −5°C before decreasing slightly as temperature nears the melting point. Heterogeneity peaks around −5°C for all three L values in consideration, and secondary peaks are found at −14, −12, and −10°C for $L = 333$ m, 1 km, and 5 km, respectively. The peaks in I at −5 and −14°C mirror previous studies that documented cloud phase transition points at similar temperatures. Danker

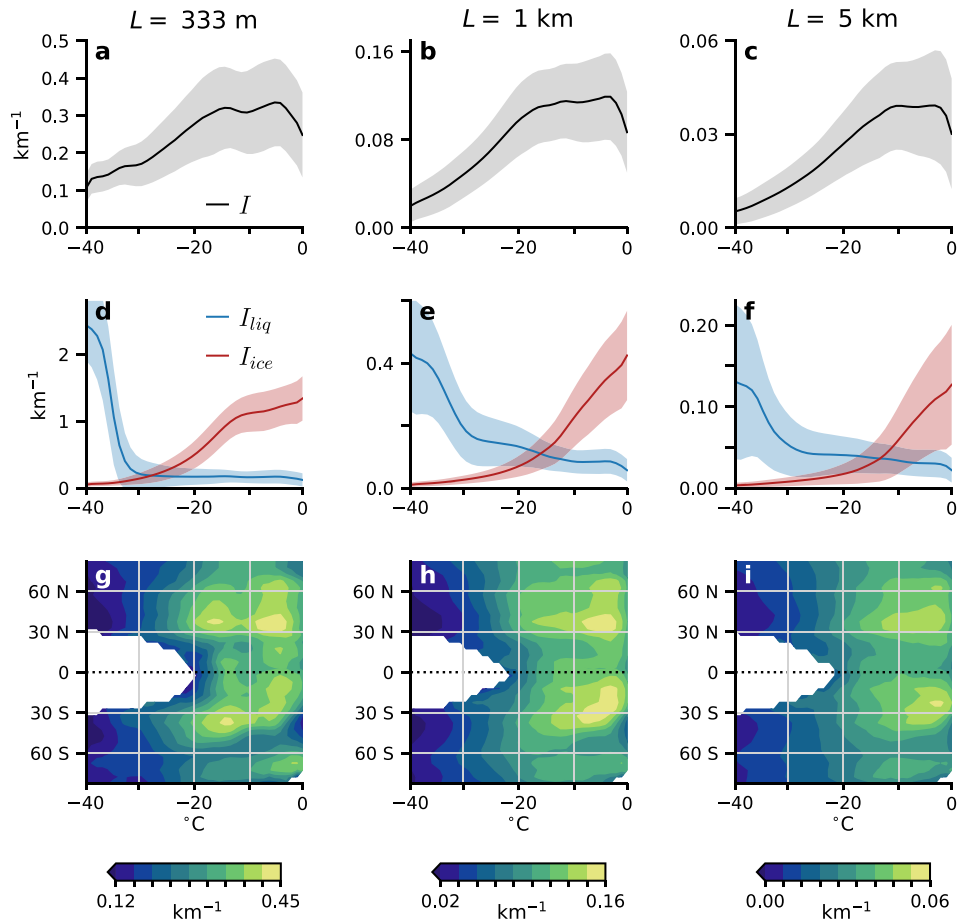

Figure 3. (a–c) Global mean I, (d–f) global mean I_{liq} and I_{ice}, and (g–i) zonal mean I as a function of temperature for retrieval averaging lengths L of (a, d) 333 m (b, e) 1 km, and (c, f) 5 km. In (a)–(f), shading shows the weighted standard deviation of all monthly mean 5° × 5°values. Values are weighted by the cloudy pixel sample size (or by the liquid/ice pixel sample size for I_{liq}/I_{ice}). In (g)–(i), data are only shown for bins containing at least 2×10^4 pixels with retrieved cloud phase. Note the varying y-axis scales in (a)–(f).

et al. (2022) examined low clouds over the SO and found a relative maximum in the frequency of mixed-phase conditions at −5°C. Moreover, they found evidence for rapid glaciation once temperatures fall below ∼−15°C, which is also supported by aircraft observations (D'Alessandro et al., 2021). Silber et al. (2021) found local minima in the occurrence of liquid in clouds over Alaska at −6 and −15°C and suggested that the minima are caused by the especially rapid vapor growth of ice at these temperatures. While I is not a direct measurement of mixed-phase conditions, the local maxima at −5 and −14°C suggests that I indeed captures the cloud phase transitions that we seek to understand.

Several aspects of Figure 3 suggest that the most heterogeneous cloud conditions are characterized by small pockets of ice within majority-liquid clouds, whereas small pockets of liquid within majority-ice clouds are rare. The clearest evidence for this is the fact that I is largest when liquid is the dominant phase: LCF = 0.8–0.9 at −5°C (Figure 1b). At this temperature, I_{ice} is significantly larger than I_{liq} (Figures 3d–3f), lending confidence that the smallest single-phase patches are indeed composed of ice. Less obviously, the shapes of the I_{liq} and I_{ice} curves in (Figures 3d–3f) also speak to the rarity of small liquid pockets within clouds that are otherwise glaciated. Starting from 0°C, I_{ice} decreases relatively gradually as temperature decreases before flattening out at ∼−20°C. The gradual change reflects a gradual increase in the size of ice-only pockets as temperature falls and more and more liquid freezes. On the other hand, I_{liq} changes very little as temperature decreases from 0 to −30°C, even as ice becomes the dominant phase. This means that liquid-only patches persisting at such cold temperatures are relatively large, allowing more liquid to remain isolated from ice. I_{liq} abruptly increases as temperature decreases from −30 to −40°C, suggesting that liquid exists primarily in small pockets only at temperatures just above the

homogeneous freezing point. These findings are broadly consistent with the expectation that the WBF process acts to quickly glaciate small liquid pockets surrounded by ice.

Above −25°C, the temperature dependence of I varies significantly with latitude, as is shown in Figures 3g–3i. In the Tropics, I is only weakly dependent on temperature. Since we are examining cloudy, sub-freezing portions of the atmosphere below 8.2 km, data from the Tropics presumably reflect tropical convective clouds that have penetrated above the freezing level. The weak temperature dependence of I in these regions may then indicate that phase heterogeneity within these clouds is relatively independent of altitude (i.e., temperature). In addition to the Tropics, I is only weakly dependent on temperature in the SO, Antarctic, and Arctic regions. This indicates that the global mean temperature dependence of I arises primarily from the mid-latitudes.

3.2. Spatial Variability

We now turn to the spatial variability of I, which is shown in Figure 4 for four 10-°C temperature bins and $L = 333$ m and 1 km (see Figure S1 in Supporting Information S1 for $L = 5$ km). As may be expected from Figures 3g–3i, these maps show that I varies substantially across the globe, even within a fixed, narrow temperature range. In general, the patterns of spatial variability found within the two warmest temperature bins are similar, but these patterns differ in many respects from those found in the two coldest temperature bins. For example, the swath of east Asia centered at (40°N, 105°E) has especially high I between −20 and 0°C but especially low I at colder temperatures.

We focus on the spatial variability of phase heterogeneity between −20 and 0°C, which is similar for $L = 333$ m and 1 km. I is largest over central and eastern Asia, western North America, central South America, and southern Africa. These heterogeneity hot spots are primarily over extratropical land and, when temperature is controlled for, have lower LCF than other regions (Figures S2 and S3 in Supporting Information S1). On the other hand, areas of especially low I are typically found over oceans, including most of the SO region between 45 and 70°S and the eastern subtropical ocean basins. These are all regions of widespread coverage of low clouds (Wood, 2012) and relatively high LCF (Figures S2 and S3 in Supporting Information S1). These patterns suggest that low clouds near the top of the marine boundary layer have a more homogeneous phase composition than other cloud types. While this may very well be true over the SO, we caution that the heterogeneity characteristics of the eastern subtropical basins should not be immediately attributed to the low stratocumulus decks that dominate those regions, since subfreezing temperatures are unlikely to occur at such low altitudes there throughout much of the year.

It is notable that I is especially low over the SO compared to similar latitudes in the northern hemisphere (NH) and other oceanic regions. The sharp gradient in I in the vicinity of the Antarctic Polar Front (APF; 50–55°S; Freeman & Lovenduski, 2016) is consistent with the previous finding that mixed-phase clouds become increasingly scarce poleward of that point (Mace et al., 2020, 2021). The causes of low heterogeneity to the south of the APF are likely complex, as changes in sea surface temperature and sea ice coverage are known to have myriad effects on boundary layer clouds (e.g., Carlsen & David, 2022; Eirund et al., 2019; Sotiropoulou et al., 2016; Young et al., 2017). Low I over the SO is also consistent with the fact that, in some models, biases in LCF and absorbed shortwave radiation are larger over the SO than in the extratropical NH (Kay et al., 2016; Tan et al., 2016; Trenberth & Fasullo, 2010). Because low I implies relatively limited contact area between liquid and ice and reduced potential for widespread WBF glaciation, the failure of models to account for subgrid phase heterogeneity would thus be expected to produce the largest LCF biases where I is low.

It is possible that some of the spatial variability in I is due to the varied availability of ice nucleating particles (INPs). INPs are aerosol particles capable of driving heterogeneous ice formation at temperatures warmer than the homogeneous freezing temperature (−38°C). By causing localized glaciation in clouds that would otherwise persist as homogeneous, supercooled liquid, INPs could plausibly affect phase heterogeneity on our lengthscales of interest. Many of the most effective INPs, such as mineral dusts, soil dusts, and certain biological particles, are emitted primarily from land (Kanji et al., 2017; Murray et al., 2012), and this could contribute to the land-sea contrast in I found here. Moreover, several of the heterogeneity hot spots seen in Figure 4—such as central Asia, central South America and the western subtropical Atlantic, and the maritime region southest of South Africa—are known regions of high concentrations of mineral dust (Adebiyi et al., 2023). If dust INPs can indeed cause elevated phase heterogeneity, the disappearance of the central Asian hot spot at temperatures below −20°C could

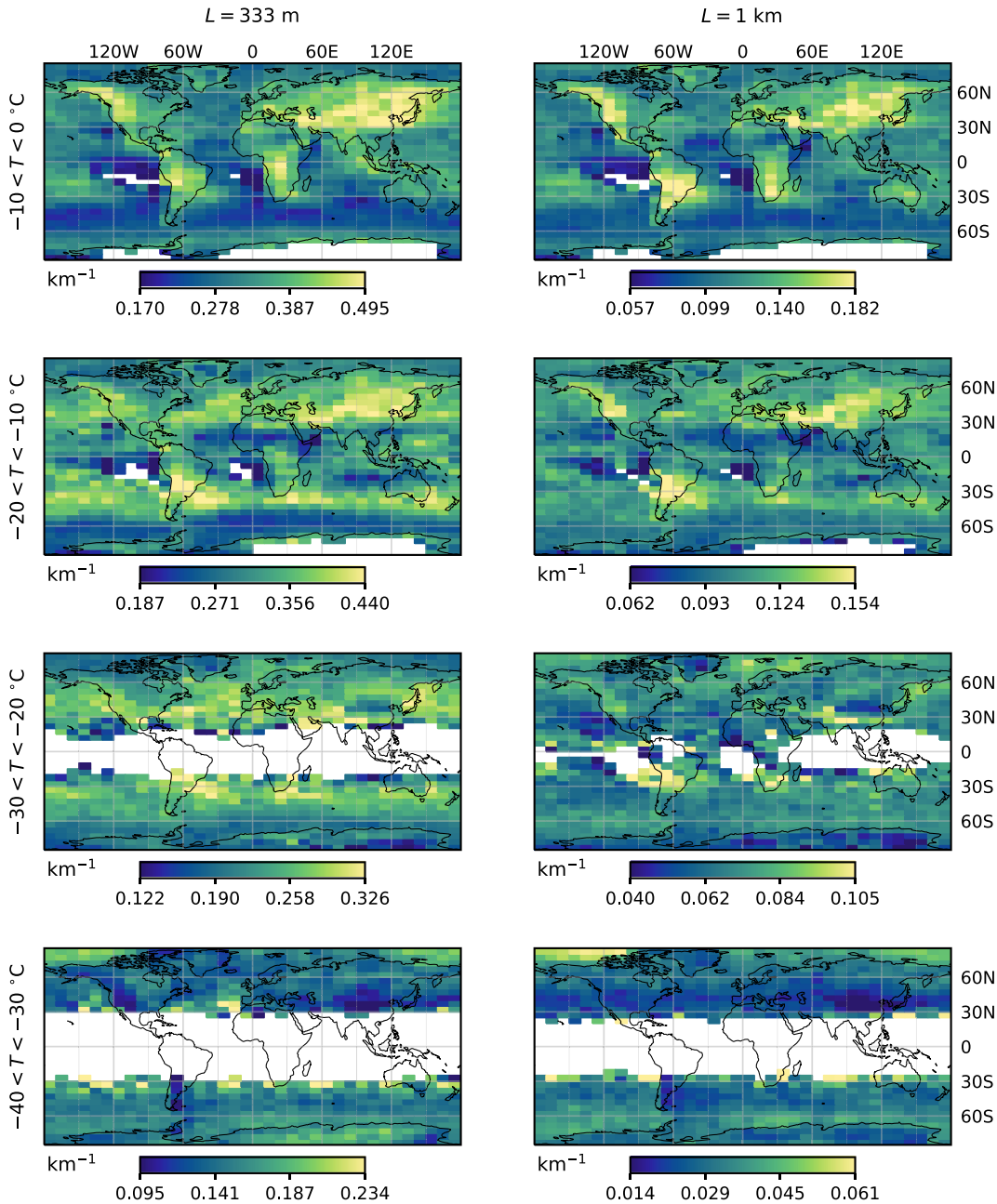

Figure 4. Mean I binned by temperature (rows; 10°C bin width) for $L = 333$ m (left) and 1 km (right). Values are only shown for grid boxes containing 2×10^4 or more cloud phase retrievals over the 3-year study period. Color scales vary for each map to highlight spatial variability. See Figure S1 in Supporting Information S1 for $L = 5$ km.

reflect the near-complete glaciation of clouds by abundant dust particles, which become more effective INPs as temperature decreases. As we shall see in the next section, seasonal variations in I also suggest that phase heterogeneity is affected by INP availability.

3.3. Annual Cycle

We now turn to the annual cycle of zonal mean I, shown in Figure 5 for four 10-°C temperature bins and $L = 333$ m and 1 km (see Figure S4 in Supporting Information S1 for $L = 5$ km). The composite annual cycle reflects the average across the 3-year study period, and we have verified that the cycle is very similar for each of the 3 years.

10.1029/2023JD039751

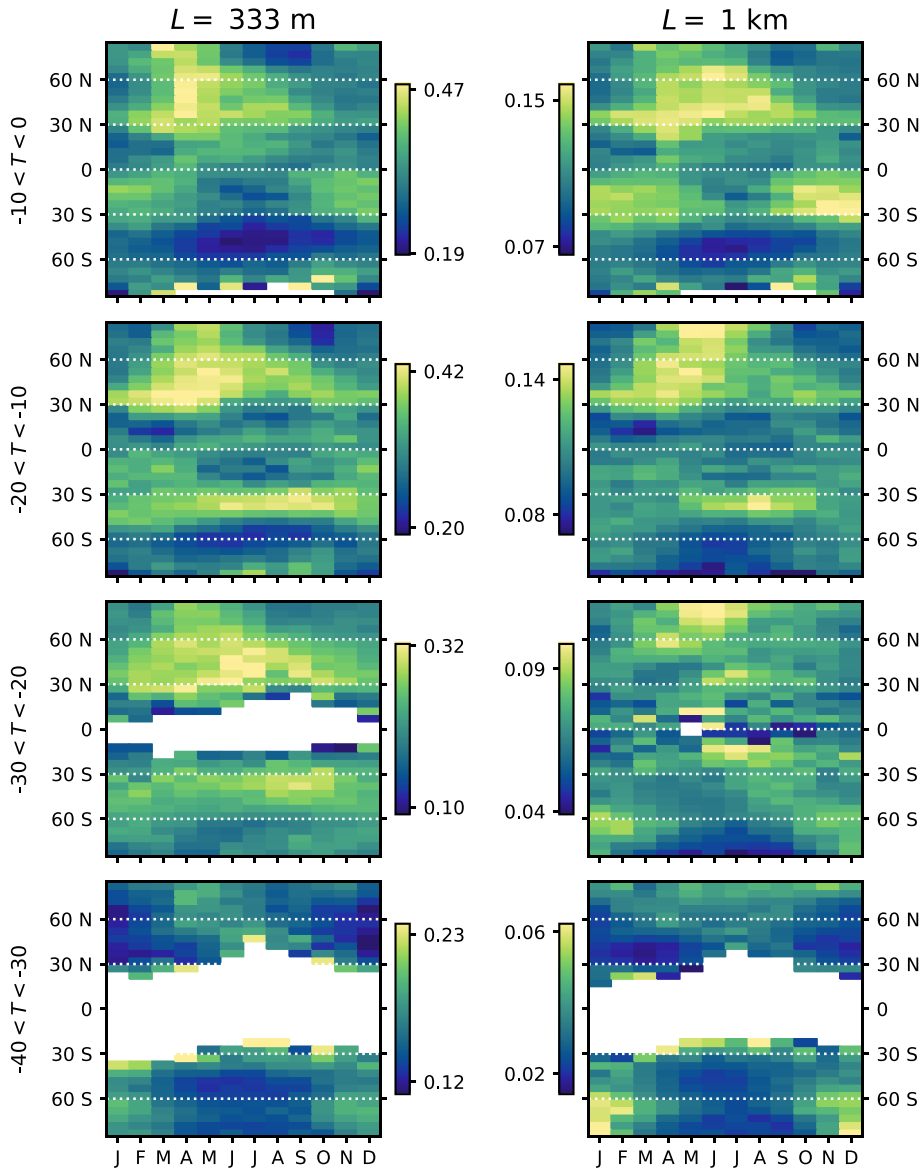

Figure 5. The annual cycle of zonal, monthly mean I (in km^{-1}) binned by temperature (rows; 10°C bin width) for $L = 333$ m (left) and 1 km (right). Data are only shown for bins containing 2×10^4 or more cloud phase retrievals. Note the different color scales for each plot, which are intended to highlight variability. The annual cycle reflects the mean over the 3-year study period. See Figure S4 in Supporting Information S1 for $L = 5$ km.

The annual cycles are similar for $L = 333$ m, 1 km, and 5 km, so we discuss them together. It is clear from Figure 5 that, even for fixed latitude, temperature, and L, I can vary significantly over the course of the year. At many latitudes, the amplitude of the annual cycle is comparable to or greater than differences between temperature bins.

The annual cycle of I throughout most of the NH extratropics is characterized by a maximum in between March and June, during boreal spring and early summer. Poleward of 60°N, I decreases throughout summer and reaches its minimum in autumn before increasing slowly throughout the winter. In the midlatitudes, I remains relatively high throughout the summer and reaches its minimum in December of January, a bit later than the polar minimum. In the tropical NH, the annual minimum occurs later still, in February or March, with a broader maximum throughout late spring and summer.

Throughout most of the Southern Hemisphere, the annual cycle of I is generally weaker in amplitude than in the NH but similarly features a peak during local spring or summer (October–February). As might be expected from

the low climatological I over the SO (Figure 4), the annual cycle of I there is modest in amplitude compared to other regions. However, the SO annual cycle is robust across different temperatures and averaging lengths, and the SO heterogeneity minimum during austral winter produces some of the lowest values of I seen around the globe. That SO phase heterogeneity is lowest during austral winter is consistent with previous work that found model LCF biases to be greatest during the same time of year (Figures 9 and 10 in Kay et al., 2016).

The spring and summertime maximum in I seen throughout the extratropics is broadly consistent with the idea that INP availability affects phase heterogeneity. Several field-based studies have found that INP concentrations in the Arctic surge after the springtime thaw of sea ice and land-based snow (Creamean et al., 2018; Tobo et al., 2019; Wex et al., 2019), and these seasonal fluctuations were recently found to affect cloud glaciation temperatures (Carlsen & David, 2022). In the SO region, I is elevated during the ice-free time of the year and depressed during the ice-covered seasons, suggesting that INPs may enhance heterogeneity there. In the Arctic, the surge in I during late spring and summer in the Arctic is aligned with the thawing of snow and sea ice, but the heterogeneity minimum in September–October, when sea ice coverage reaches its annual minimum, suggests that the relationship between heterogeneity and Arctic sea ice and snow cover is not straightforward.

A major exception to the spring and summertime heterogeneity maximum is found just north of the APF (30–45°S) for $-30 < T < -10$°C. Here, I is greatest during austral winter. The relatively abrupt shift in the timing of the annual cycle across the APF is aligned with the abrupt change in annual mean I there and is yet another piece of evidence suggesting that cloud phase characteristics change dramatically across the APF. Explaining the shift in the timing of the annual cycle of may be a worthwhile endeavor but is beyond our scope here.

4. Discussion

This paper presents, to our knowledge, the first global assessment of cloud phase heterogeneity using spaceborne satellite measurements. The most heterogeneous cloud phase conditions, characterized by the presence of small ice pockets within majority-liquid clouds, are found between −15 and −5°C and tend to occur over midlatitude land. Phase tends to be more homogeneous over cloudy maritime regions such as the SO and the eastern subtropical basins. The annual cycle of phase heterogeneity depends on temperature and location but is generally characterized by a minimum during local winter and a maximum during local spring or summer. While the patterns of variability found here are informative, phase heterogeneity is clearly affected by factors other than temperature, location, and time of year. One such factor may be the availability of INPs; our results suggest that phase heterogeneity is greater during times of year when INP emissions are thought to be elevated. The relationship between INP availability and phase heterogeneity is surely complex and, at this point, is only speculative. Future work may focus more on this subject and on understanding how heterogeneity is affected by factors such as cloud type, cloud dynamics, and thermodynamic conditions.

The use of spaceborne lidar to study phase heterogeneity has many limitations. In addition to the lack of a mixed-phase classification and the complications arising from CALIOP's multigridded averaging scheme (Section 2.1), the lidar signal attenuates at an optical depth of ∼5 (Winker et al., 2009), which means that our results are skewed to represent conditions near cloud top. Furthermore, about 17% of the cloud observations in our study period lacked a high- or medium-quality phase determination and were not included in our analysis. We reiterate that we have neglected vertical phase heterogeneity here, which may be a significant source of liquid-ice interface area over the SO (e.g., Alexander et al., 2021). Lastly, we draw attention to the sources of error discussed in Mace et al. (2021), who demonstrated the difficulty of observing mixed-phase clouds using spaceborne lidar. In particular, they documented the presence of low clouds over the SO that are mixed-phase but appear to spaceborne lidar as supercooled liquid because the layer scattering characteristics are heavily dominated by liquid droplets. The inability of spaceborne lidar to identify the presence of ice in such clouds is an inherent limitation of our methodology.

Despite these significant limitations, the patterns of phase heterogeneity captured by our metric, I, are largely consistent with expectations from previous work. The temperature dependence of I features transition points that have been documented previously (Section 3.1), and the climatological and seasonal variability of I over the SO is consistent with expectations from studies of model LCF bias (Sections 3.2 and 3.3). Thus, while the I metric used here is far from perfect, it is presumably able to capture real variability in cloud phase characteristics. These successes add credence to the use of spaceborne observations to bridge the gap between high-resolution,

limited-area aircraft data and the global scales on which GCMs operate. The ability of lidar observations to characterize phase heterogeneity on scales much smaller than a GCM grid box presents a valuable opportunity to improve model representations of mixed-phase microphysics and address longstanding model biases related to clouds and radiation.

Future work will focus on how to meaningfully convert satellite-derived I to a scaling parameter that can be used to adjust WBF efficiency in the microphysics parameterizations used in GCMs. Based on the results presented here, it would be wise for these implementations to account for the dependence of phase heterogeneity on temperature, latitude, and time of year. Any implementation must also consider the fact that I is a measure of liquid-ice interface density at a fixed vertical level along a one-dimensional satellite track; even if vertical phase heterogeneity is to be neglected, I must still be generalized from one horizontal dimension to two. Approaches may vary from model to model due to differences in grid type and WBF parameterizations, and for this reason we leave the details of such implementation for future work.

Data Availability Statement

The CALIOP Vertical Feature Mask and L2 Cloud Profile products used in this study are publicly available at (NASA/LARC/SD/ASDC, 2018a, 2018b). The global data set of phase heterogeneity statistics computed for this paper and used to make the figures has been made publicly available (Sokol & Storelvmo, 2023).

Acknowledgments
We thank three anonymous reviewers for their constructive feedback. This work was supported by the European Research Council (ERC) through Grants StG 758005 and CoG 101045273.

References

Adebiyi, A., Kok, J. F., Murray, B. J., Ryder, C. L., Stuut, J.-B. W., Kahn, R. A., et al. (2023). A review of coarse mineral dust in the Earth system. *Aeolian Research*, *60*, 100849. https://doi.org/10.1016/j.aeolia.2022.100849

Alexander, S. P., McFarquhar, G. M., Marchand, R., Protat, A., Vignon, É., Mace, G. G., & Klekociuk, A. R. (2021). Mixed-phase clouds and precipitation in Southern Ocean cyclones and cloud systems observed poleward of 64°S by ship-based cloud radar and lidar. *Journal of Geophysical Research: Atmospheres*, *126*(8), e2020JD033626. https://doi.org/10.1029/2020JD033626

Atlas, R., Mohrmann, J., Finlon, J., Lu, J., Hsiao, I., Wood, R., & Diao, M. (2021). The University of Washington Ice–Liquid Discriminator (UWILD) improves single-particle phase classifications of hydrometeors within Southern Ocean clouds using machine learning. *Atmospheric Measurement Techniques*, *14*(11), 7079–7101. https://doi.org/10.5194/amt-14-7079-2021

Avery, M. A., Ryan, R. A., Getzewich, B. J., Vaughan, M. A., Winker, D. M., Hu, Y., et al. (2020). CALIOP V4 cloud thermodynamic phase assignment and the impact of near-nadir viewing angles. *Atmospheric Measurement Techniques*, *13*(8), 4539–4563. https://doi.org/10.5194/amt-13-4539-2020

Baumgardner, D., Abel, S. J., Axisa, D., Cotton, R., Crosier, J., Field, P., et al. (2017). Cloud ice properties: In situ measurement challenges. *Meteorological Monographs*, *58*(1), 9.1–9.23. https://doi.org/10.1175/AMSMONOGRAPHS-D-16-0011.1

Bergeron, T. (1928). Über die dreidimensional verknüpfende Wetteranalyse. *Geophysica Norvegica*, *5*, 1–111.

Carlsen, T., & David, R. O. (2022). Spaceborne evidence that ice-nucleating particles influence high-latitude cloud phase. *Geophysical Research Letters*, *49*(14), e2022GL098041. https://doi.org/10.1029/2022GL098041

Cesana, G., Chepfer, H., Winker, D., Getzewich, B., Cai, X., Jourdan, O., et al. (2016). Using in situ airborne measurements to evaluate three cloud phase products derived from CALIPSO. *Journal of Geophysical Research: Atmospheres*, *121*(10), 5788–5808. https://doi.org/10.1002/2015JD024334

Cesana, G., Waliser, D. E., Jiang, X., & Li, J.-L. F. (2015). Multimodel evaluation of cloud phase transition using satellite and reanalysis data. *Journal of Geophysical Research: Atmospheres*, *120*(15), 7871–7892. https://doi.org/10.1002/2014JD022932

Choi, Y.-S., Ho, C.-H., Park, C.-E., Storelvmo, T., & Tan, I. (2014). Influence of cloud phase composition on climate feedbacks. *Journal of Geophysical Research: Atmospheres*, *119*(7), 3687–3700. https://doi.org/10.1002/2013JD020582

Chylek, P., & Borel, C. (2004). Mixed phase cloud water/ice structure from high spatial resolution satellite data. *Geophysical Research Letters*, *31*(14), L14104. https://doi.org/10.1029/2004GL020428

Creamean, J. M., Kirpes, R. M., Pratt, K. A., Spada, N. J., Maahn, M., de Boer, G., et al. (2018). Marine and terrestrial influences on ice nucleating particles during continuous springtime measurements in an Arctic oilfield location. *Atmospheric Chemistry and Physics*, *18*(24), 18023–18042. https://doi.org/10.5194/acp-18-18023-2018

D'Alessandro, J. J., Diao, M., Wu, C., Liu, X., Jensen, J. B., & Stephens, B. B. (2019). Cloud phase and relative humidity distributions over the Southern Ocean in austral summer based on in situ observations and CAM5 simulations. *Journal of Climate*, *32*(10), 2781–2805. https://doi.org/10.1175/JCLI-D-18-0232.1

D'Alessandro, J. J., McFarquhar, G. M., Wu, W., Stith, J. L., Jensen, J. B., & Rauber, R. M. (2021). Characterizing the occurrence and spatial heterogeneity of liquid, ice, and mixed phase low-level clouds over the Southern Ocean using in situ observations acquired during SOCRATES. *Journal of Geophysical Research: Atmospheres*, *126*(11), e2020JD034482. https://doi.org/10.1029/2020JD034482

Danker, J., Sourdeval, O., McCoy, I. L., Wood, R., & Possner, A. (2022). Exploring relations between cloud morphology, cloud phase, and cloud radiative properties in Southern Ocean's stratocumulus clouds. *Atmospheric Chemistry and Physics*, *22*(15), 10247–10265. https://doi.org/10.5194/acp-22-10247-2022

Eirund, G. K., Possner, A., & Lohmann, U. (2019). Response of Arctic mixed-phase clouds to aerosol perturbations under different surface forcings. *Atmospheric Chemistry and Physics*, *19*(15), 9847–9864. https://doi.org/10.5194/acp-19-9847-2019

Field, P. R., Hogan, R. J., Brown, P. R. A., Illingworth, A. J., Choularton, T. W., Kaye, P. H., et al. (2004). Simultaneous radar and aircraft observations of mixed-phase cloud at the 100 m scale. *Quarterly Journal of the Royal Meteorological Society*, *130*(600), 1877–1904. https://doi.org/10.1256/qj.03.102

Findeisen, W. (1938). Die kolloidmeteorologischen Vorgänge bei der Niederschlagsbildung (E. Volken, A. M. Giesche, & S. Brönnimann, Trans.). *Meteorologische Zeitschrift*, *55*, 121–133. https://doi.org/10.1127/metz/2015/0675

Freeman, N. M., & Lovenduski, N. S. (2016). Mapping the Antarctic Polar Front: Weekly realizations from 2002 to 2014. *Earth System Science Data*, *8*(1), 191–198. https://doi.org/10.5194/essd-8-191-2016

Frey, W. R., & Kay, J. E. (2018). The influence of extratropical cloud phase and amount feedbacks on climate sensitivity. *Climate Dynamics*, *50*(7), 3097–3116. https://doi.org/10.1007/s00382-017-3796-5

Hu, Y., Winker, D., Vaughan, M., Lin, B., Omar, A., Trepte, C., et al. (2009). CALIPSO/CALIOP cloud phase discrimination algorithm. *Journal of Atmospheric and Oceanic Technology*, *26*(11), 2293–2309. https://doi.org/10.1175/2009JTECHA1280.1

Huang, Y., Dong, X., Kay, J. E., Xi, B., & McIlhattan, E. A. (2021). The climate response to increased cloud liquid water over the Arctic in CESM1: A sensitivity study of Wegener–Bergeron–Findeisen process. *Climate Dynamics*, *56*(9), 3373–3394. https://doi.org/10.1007/s00382-021-05648-5

Kanji, Z. A., Ladino, L. A., Wex, H., Boose, Y., Burkert-Kohn, M., Cziczo, D. J., & Krämer, M. (2017). Overview of ice nucleating particles. *Meteorological Monographs*, *58*(1), 1.1–1.33. https://doi.org/10.1175/AMSMONOGRAPHS-D-16-0006.1

Kay, J. E., Bourdages, L., Miller, N. B., Morrison, A., Yettella, V., Chepfer, H., & Eaton, B. (2016). Evaluating and improving cloud phase in the Community Atmosphere Model version 5 using spaceborne lidar observations. *Journal of Geophysical Research: Atmospheres*, *121*(8), 4162–4176. https://doi.org/10.1002/2015JD024699

Komurcu, M., Storelvmo, T., Tan, I., Lohmann, U., Yun, Y., Penner, J. E., et al. (2014). Intercomparison of the cloud water phase among global climate models. *Journal of Geophysical Research: Atmospheres*, *119*(6), 3372–3400. https://doi.org/10.1002/2013JD021119

Korolev, A., Isaac, G. A., Cober, S. G., Strapp, J. W., & Hallett, J. (2003). Microphysical characterization of mixed-phase clouds. *Quarterly Journal of the Royal Meteorological Society*, *129*(587), 39–65. https://doi.org/10.1256/qj.01.204

Korolev, A., McFarquhar, G., Field, P. R., Franklin, C., Lawson, P., Wang, Z., et al. (2017). Mixed-phase clouds: Progress and challenges. *Meteorological Monographs*, *58*(1), 5.1–5.50. https://doi.org/10.1175/AMSMONOGRAPHS-D-17-0001.1

Mace, G. G., Benson, S., & Hu, Y. (2020). On the frequency of occurrence of the ice phase in supercooled Southern Ocean Low clouds derived from CALIPSO and CloudSat. *Geophysical Research Letters*, *47*(14), e2020GL087554. https://doi.org/10.1029/2020GL087554

Mace, G. G., Protat, A., & Benson, S. (2021). Mixed-phase clouds over the Southern Ocean as observed from satellite and surface based lidar and radar. *Journal of Geophysical Research: Atmospheres*, *126*(16), e2021JD034569. https://doi.org/10.1029/2021JD034569

McFarquhar, G. M., Um, J., & Jackson, R. (2013). Small cloud particle shapes in mixed-phase clouds. *Journal of Applied Meteorology and Climatology*, *52*(5), 1277–1293. https://doi.org/10.1175/JAMC-D-12-0114.1

McIlhattan, E. A., L'Ecuyer, T. S., & Miller, N. B. (2017). Observational evidence linking Arctic supercooled liquid cloud biases in CESM to snowfall processes. *Journal of Climate*, *30*(12), 4477–4495. https://doi.org/10.1175/JCLI-D-16-0666.1

Mitchell, J. F. B., Senior, C. A., & Ingram, W. J. (1989). $C0_2$ and climate: A missing feedback? *Nature*, *341*(6238), 132–134. https://doi.org/10.1038/341132a0

Murray, B. J., O'Sullivan, D., Atkinson, J. D., & Webb, M. E. (2012). Ice nucleation by particles immersed in supercooled cloud droplets. *Chemical Society Reviews*, *41*(19), 6519–6554. https://doi.org/10.1039/C2CS35200A

NASA/LARC/SD/ASDC. (2018a). CALIPSO Lidar Level 2 Cloud Profile, V4-20 [Dataset]. NASA Langley Atmospheric Science Data Center DAAC. https://doi.org/10.5067/CALIOP/CALIPSO/LID_L2_05KMCPRO-STANDARD-V4-20

NASA/LARC/SD/ASDC. (2018b). CALIPSO Lidar Level 2 Vertical Feature Mask (VFM), V4-20 [Dataset]. NASA Langley Atmospheric Science Data Center DAAC. https://doi.org/10.5067/CALIOP/CALIPSO/CAL_LID_L2_VFM-Standard-V4-21

Sherwood, S. C., Webb, M. J., Annan, J. D., Armour, K. C., Forster, P. M., Hargreaves, J. C., et al. (2020). An assessment of Earth's climate sensitivity using multiple lines of evidence. *Reviews of Geophysics*, *58*(4), e2019RG000678. https://doi.org/10.1029/2019RG000678

Silber, I., McGlynn, P. S., Harrington, J. Y., & Verlinde, J. (2021). Habit-dependent vapor growth modulates Arctic supercooled water occurrence. *Geophysical Research Letters*, *48*(10), e2021GL092767. https://doi.org/10.1029/2021GL092767

Sokol, A. B., & Storelvmo, T. (2023). Data to accompany "The spatial heterogeneity of cloud phase observed by satellite". *ResearchWorks Archive*. Retrieved from http://hdl.handle.net/1773/50048

Sotiropoulou, G., Tjernström, M., Sedlar, J., Achtert, P., Brooks, B. J., Brooks, I. M., et al. (2016). Atmospheric conditions during the Arctic Clouds in Summer Experiment (ACSE): Contrasting open water and sea ice surfaces during melt and freeze-up seasons. *Journal of Climate*, *29*(24), 8721–8744. https://doi.org/10.1175/JCLI-D-16-0211.1

Storelvmo, T., Tan, I., & Korolev, A. V. (2015). Cloud phase changes induced by CO_2 warming—A powerful yet poorly constrained cloud-climate feedback. *Current Climate Change Reports*, *1*(4), 288–296. https://doi.org/10.1007/s40641-015-0026-2

Tan, I., & Storelvmo, T. (2016). Sensitivity study on the influence of cloud microphysical parameters on mixed-phase cloud thermodynamic phase partitioning in CAM5. *Journal of the Atmospheric Sciences*, *73*(2), 709–728. https://doi.org/10.1175/JAS-D-15-0152.1

Tan, I., Storelvmo, T., & Zelinka, M. D. (2016). Observational constraints on mixed-phase clouds imply higher climate sensitivity. *Science*, *352*(6282), 224–227. https://doi.org/10.1126/science.aad5300

Thompson, D. R., Kahn, B. H., Green, R. O., Chien, S. A., Middleton, E. M., & Tran, D. Q. (2018). Global spectroscopic survey of cloud thermodynamic phase at high spatial resolution, 2005–2015. *Atmospheric Measurement Techniques*, *11*(2), 1019–1030. https://doi.org/10.5194/amt-11-1019-2018

Tobo, Y., Adachi, K., DeMott, P. J., Hill, T. C. J., Hamilton, D. S., Mahowald, N. M., et al. (2019). Glacially sourced dust as a potentially significant source of ice nucleating particles. *Nature Geoscience*, *12*(4), 253–258. https://doi.org/10.1038/s41561-019-0314-x

Trenberth, K. E., & Fasullo, J. T. (2010). Simulation of present-day and twenty-first-century energy budgets of the Southern Oceans. *Journal of Climate*, *23*(2), 440–454. https://doi.org/10.1175/2009JCLI3152.1

Tsushima, Y., Emori, S., Ogura, T., Kimoto, M., Webb, M. J., Williams, K. D., et al. (2006). Importance of the mixed-phase cloud distribution in the control climate for assessing the response of clouds to carbon dioxide increase: A multi-model study. *Climate Dynamics*, *27*(2), 113–126. https://doi.org/10.1007/s00382-006-0127-7

Vaughan, M. A., Powell, K. A., Winker, D. M., Hostetler, C. A., Kuehn, R. E., Hunt, W. H., et al. (2009). Fully automated detection of cloud and aerosol layers in the CALIPSO lidar measurements. *Journal of Atmospheric and Oceanic Technology*, *26*(10), 2034–2050. https://doi.org/10.1175/2009JTECHA1228.1

Vaughan, M. A., Winker, D. M., & Powell, K. A. (2005). CALIOP algorithm theoretical basis document Part 2: Feature detection and layer properties algorithms. Retrieved from https://www-calipso.larc.nasa.gov/resources/pdfs/PC-SCI-202_Part2_rev1x01.pdf

Wegener, A. (1911). *Thermodynamik der Atmosphäre*. J.A. Barth.

Wex, H., Huang, L., Zhang, W., Hung, H., Traversi, R., Becagli, S., et al. (2019). Annual variability of ice-nucleating particle concentrations at different Arctic locations. *Atmospheric Chemistry and Physics*, *19*(7), 5293–5311. https://doi.org/10.5194/acp-19-5293-2019

Winker, D. M., Vaughan, M. A., Omar, A., Hu, Y., Powell, K. A., Liu, Z., et al. (2009). Overview of the CALIPSO mission and CALIOP data processing algorithms. *Journal of Atmospheric and Oceanic Technology*, *26*(11), 2310–2323. https://doi.org/10.1175/2009JTECHA1281.1

Wood, R. (2012). Stratocumulus clouds. *Monthly Weather Review*, *140*(8), 2373–2423. https://doi.org/10.1175/MWR-D-11-00121.1

Young, G., Connolly, P. J., Jones, H. M., & Choularton, T. W. (2017). Microphysical sensitivity of coupled springtime Arctic stratocumulus to modelled primary ice over the ice pack, marginal ice, and ocean. *Atmospheric Chemistry and Physics*, *17*(6), 4209–4227. https://doi.org/10.5194/acp-17-4209-2017

Zelinka, M. D., Myers, T. A., McCoy, D. T., Po-Chedley, S., Caldwell, P. M., Ceppi, P., et al. (2020). Causes of higher climate sensitivity in CMIP6 models. *Geophysical Research Letters*, *47*(1), e2019GL085782. https://doi.org/10.1029/2019GL085782

Zhang, M., Liu, X., Diao, M., D'Alessandro, J. J., Wang, Y., Wu, C., et al. (2019). Impacts of representing heterogeneous distribution of cloud liquid and ice on phase partitioning of Arctic mixed-phase clouds with NCAR CAM5. *Journal of Geophysical Research: Atmospheres*, *124*(23), 13071–13090. https://doi.org/10.1029/2019JD030502